

# Mesoscale FEM Model of Concrete: Statistical Assessment of Inherent Stress Concentrations in Dependence on Phase Heterogeneity

Jan Mašek<sup>a,b</sup>, Petr Miarka<sup>a,b</sup>

<sup>a</sup>*Institute of Physics of Materials,  
Czech Academy of Sciences, Žitkova 22, 616 00 Brno, Czech Republic,  
e-mail: masek@ipm.cz, miarka@ipm.cz*

<sup>b</sup>*Institute of Structural Mechanics,  
Faculty of Civil Engineering, Brno University of Technology, Veveří 331/95, 602 00 Brno, Czech Republic,  
e-mail: jan.masek1@vut.cz, petr.miarka@vut.cz*

arXiv:2506.16242v1 [cond-mat.mtrl-sci] 19 Jun 2025

---

## Abstract

Concrete heterogeneity originates from its production process, which involves bonding aggregates with a binder matrix. This study presents a mesoscale finite element model (MFEM) that offers detailed insights into the fracture process at the aggregate–cement matrix interface, focusing on one of concrete’s key properties: its mechanical response. Unlike discrete models, which often average out critical stress concentrations within the mesostructure, the MFEM approach captures detailed stress distributions, revealing localized effects crucial for understanding damage evolution. Although computationally more demanding, the MFEM leverages modern high-performance computing (HPC) to provide a detailed description of the stress field and material damage across different phases and interfaces.

Various matrix-to-aggregate stiffness ratios are considered to evaluate the influence of material heterogeneity on the stress field. The results are based on a statistical evaluation of stress concentrations arising from variations in material stiffness. The model is applied to investigate the impact of using recycled crushed bricks as aggregates in concrete, with particular emphasis on the stiffness mismatch between the matrix and aggregates. The study examines how this stiffness contrast affects stress distribution and ultimately influences the composite’s failure mechanisms.

*Keywords:*

MFEM, meso-scale, concrete, heterogeneity, aggregate-cement interface, stiffness mismatch, recycled aggregates

---

## 1. Introduction

Concrete is one of the most widely used construction materials worldwide due to its structural versatility, shape variability, and long-term durability. From a continuum mechanics perspective, concrete is a heterogeneous material, with the origin of its heterogeneity rooted in the production process, which involves binding aggregates together with a binder—typically granite aggregates combined with Portland cement [1]. In structural applications, however, concrete is usually treated as a homogeneous material, with its mechanical properties defined according to established standards [2].

Nevertheless, this inherent heterogeneity becomes apparent at smaller scales, where it can significantly influence the initiation of damage. More specifically, concrete is a multi-phase material, with the number and nature of its phases depending on the scale under investigation [3]. At the aggregate scale, three distinct phases can be

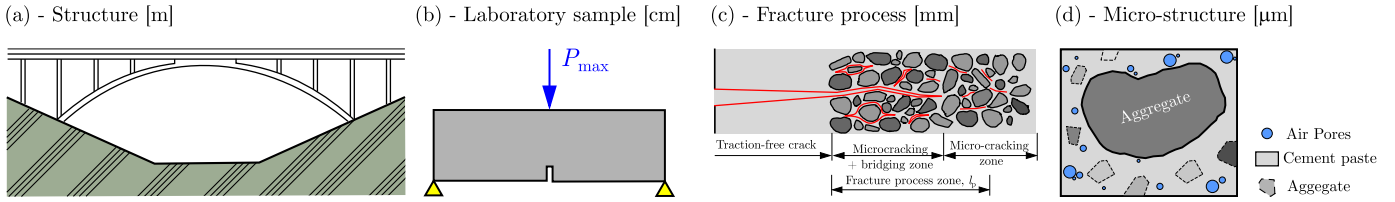


Figure 1: Scales of analysis of concrete structures.

identified: aggregates, cement paste, and air pores. Additionally, a fourth phase—the interfacial transition zone (ITZ)—represents the bonding behavior between the aggregates and the cement paste [4]. The differences in concrete material scales are illustrated in Figure 1.

The number of phases depends on the investigated scale. For structural applications, it is beneficial to use homogenized behavior, whereas for processes occurring at the aggregate–cement matrix level, a multi-phase material model is necessary to accurately describe the observed behavior [5]. This inherent heterogeneity poses a challenge for accurately calculating stresses, which are crucial for predicting future failure under both static and cyclic loading conditions.

Significant effort has been invested in developing numerical models of the mechanical response of concrete and formulating constitutive laws, which allow for more accurate predictions of stress and subsequent damage. The most common material models are typically formulated in tensorial form within the classical continuum theory, such as the Concrete Damage Plasticity Model [6], the Fracture-Plastic Constitutive Model [7] implemented in ATENA software, microplane models [8, 9], and phase-field models [10]. These models treat the material as macroscopically homogeneous without explicitly accounting for lower-scale heterogeneity.

In contrast to the constitutive material models, meso-scale models of concrete directly involve individual heterogeneous units [11], which arise from the combination of a constitutive relation at a mesoscale and explicitly modelled material structure [12]. The meso-scale model can provide the information about the fracture processes at the level of aggregate to cement matrix bond [13]. Thus, it can properly describe the most prominent concrete’s disadvantage, i.e. the strain-softening behaviour as a response to the tensile load [4]. Besides continuum-based models, there exists multiple other solutions such as lattice discrete particle model (LDPM) [14] or discrete finite element method (DFEM) [15], where the interconnectivity of each particle has its defined interaction. On the other hand, the use of meso-scale finite element method (MFEM) model without the defined interaction can be employed for the stress calculations as well.

The engineering practice often desires more simple solutions than using sophisticated and often computationally expensive model. The structural design of concrete load bearing structure is using well acknowledged linear elastic beam theory often called Euler-Bernoulli’s theory for stress and deformation calculations, unfortunately without accounting for this high heterogeneity of concrete. The stress is then adjusted based on design recommendations in standards based on empirical or experimental observations [16]. Figure 2 compares bending stress calculated using various methods. It shows an example of how different computational approaches can simplify the stress calculation.

As shown in Figure 2, once the analyzed component contains a defect, the stress calculation must be adjusted to account for the stress distribution changes along the height. Stress concentration arising from this defect can be addressed using the linear elastic fracture mechanics (LEFM) approach [17], which is commonly applied in studies of metals due to strong experimental support [18] and extensive documentation in handbooks.

In the case of nonlinear material (NLM) behavior, the resulting stress at the defect location does not exceed the

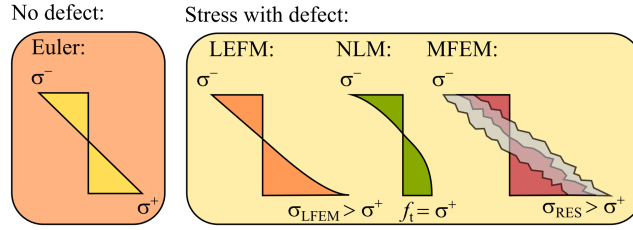


Figure 2: Illustration of normal stress caused by bending obtained by multiple calculation methods.

material’s tensile strength [6], and the damage is distributed (smeared) over the region of high stresses [19]. After reaching the tensile strength  $f_t$ , smeared cracking behavior is assumed, characterized by a maximum tensile strain  $\varepsilon_t$  usually related to the crack width  $w_c$ . In contrast, the MFEM model accounts for local stress concentrations not only from the defect but also from the aggregate’s shape and mechanical properties.

This numerical study investigates mechanical stress distribution through 3D MFEM simulations under different loading conditions and model geometries. These include three-point bending tests on both notched and unnotched beams to induce bending stresses, as well as a compressed cylinder representing a pure compression state. Various matrix-to-aggregate stiffness ratios are considered to evaluate the influence of material heterogeneity on the stress field. The results are based on a statistical evaluation of stress concentrations arising from variations in material stiffness.

## 2. Motivation

The use of crushed brick as a replacement for natural aggregates in concrete offers both environmental and economic advantages. However, concerns remain regarding its mechanical performance, particularly due to the stiffness mismatch between brick aggregates and the cement matrix. Unlike granite aggregate concrete—where a uniform stiffness is often assumed based on empirical reliability—brick aggregate concrete exhibits a pronounced contrast in elastic properties. This discrepancy leads to stress concentrations at the aggregate-matrix interfaces, which can accelerate microcrack initiation and alter the overall stress distribution within the material [20, 21]. Understanding these variations in the stress field is crucial, as they directly influence crack propagation mechanisms and ultimately affect the structural integrity of the composite.

Recycled materials, including crushed bricks, are increasingly employed as coarse aggregates in concrete [22]. The incorporation of aggregates with mechanical properties significantly different from traditional materials such as granite can substantially impact the mechanical response of the composite [23]. In particular, stress concentration zones become critical, serving as initiation points for material damage and failure. Brick aggregates present additional complexities due to their inherent variability. Their material properties can vary considerably [24], with reported elastic modulus values ranging from 3.5 GPa to 34 GPa and Poisson’s ratios between 0.12 and 0.29. Moreover, the crushing process may introduce further degradation, increasing heterogeneity among individual aggregates. This variability complicates the mechanical behavior of brick aggregate concrete, necessitating a deeper investigation into its stress distribution and failure mechanisms.

This study aims to examine the evolution of stress concentrations and damage initiation in crushed brick aggregate concrete, providing insights into its mechanical limitations and exploring potential strategies for performance improvement.

### 3. Modeling approach

In what follows, we introduce the method selected for heterogeneous topology generation, which is based on Voronoi tessellation and its adjustments for meso-structure generation informed by the material's sieve curve. Next, the numerical model is presented, including geometry, topology, and FE mesh generation.

#### 3.1. Meso-structure topology generation

To model the heterogeneous structure of classical concrete, we first focus on capturing the shape and distribution of the aggregates. Figure 3a shows a typical concrete mesostructure containing granite aggregates embedded in a cement matrix. The shape of the aggregates depends on the material and origin of the aggregate source. However, aggregates often resemble sharp-edged convex polyhedra (e.g., crushed granite or crushed brick recycle). Therefore, without excessive simplification, it is reasonable to utilize convex polyhedral shapes within numerical models. Figure 3b illustrates how convex polyhedra can be identified in the depicted concrete mesostructure.



Figure 3: a) A typical concrete mesostructure, b) a possible approximation of aggregates by convex polyhedra.

The generation of the mesostructure begins with conducting a tessellation on a set of generating nodes. All figures in Figure 4 present a 2D illustration of the mesostructure generation process. A classic Voronoi cell,  $C_i$ , contains all domain points,  $\mathbf{u}$ , that are closer to the respective generating node  $\mathbf{X}_i$  than to any other generating node  $\mathbf{X}_k$  in the model domain,  $\Omega$ :

$$C_i = \{\mathbf{u} \in \Omega \mid \forall k \neq i \quad \|\mathbf{u} - \mathbf{X}_i\| < \|\mathbf{u} - \mathbf{X}_k\|\} \quad (1)$$

Unlike the classic Voronoi tessellation, we utilize the Power diagram variant [25]. The Power diagram is a weighted version of the standard Voronoi tessellation, where each cell,  $P_i$ , encompasses all domain points associated with a sphere of radius  $r_i$  around its generating node  $\mathbf{X}_i$ :

$$P_i = \{\mathbf{u} \in \Omega \mid \forall k \neq i \quad \|\mathbf{u} - \mathbf{X}_i\|^2 - r_i^2 < \|\mathbf{u} - \mathbf{X}_k\|^2 - r_k^2\} \quad (2)$$

This approach enables an uneven distribution of Voronoi cell sizes that approximates a Fuller curve from  $l_{\min}$  to  $l_{\max}$ , as illustrated in Figure 4a.

The model geometry is created by randomly sequentially placing nodes into the volume domain of the intended model,  $\Omega$ . We restrict the mutual distance between nodes,  $d$ , to lie within the range  $d_{\min} \leq d \leq d_{\max}$ . The generator starts with the maximum interparticle distance  $d = d_{\max}$  and randomly places nodes into the domain, ensuring that no two nodes are closer than  $d$ . After  $10^5$  consecutive failed placement attempts, the algorithm decreases  $d$  to the next smaller value on the Fuller curve and repeats the process. The generation ends upon reaching a target domain saturation,  $S_{\text{target}}$ , typically set to 95%.

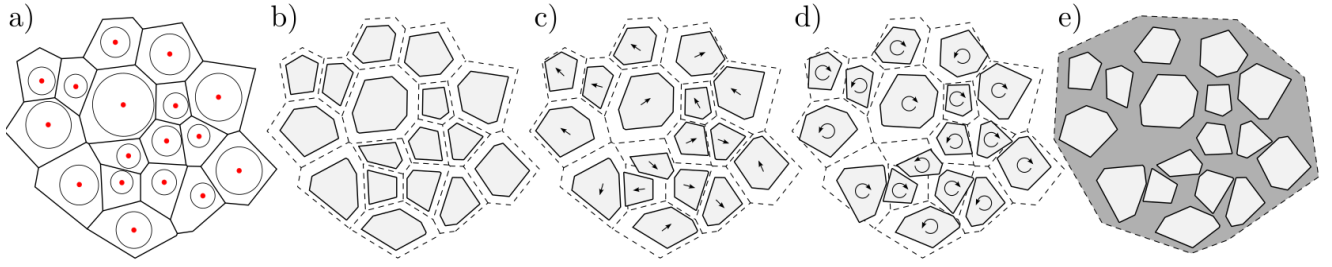


Figure 4: An illustration of the mesostructure generation process: a) Power diagram of the input nodes, b) shrinking the cells (aggregates) towards their center of gravity to create the matrix volume, c) a random translation of the cells, d) random rotation of the cells, e) the resulting mesostructure with aggregates and cement matrix.

To create a heterogeneous mesostructure resembling generic concrete, we shrink the cells toward their respective centers of gravity, creating intermediate zones that will eventually contain the cement matrix (see Figure 4b). The minimal distance of generating nodes and their radii during initial node placement reflect this shrinking so that the final grains have the intended size. Depending on the expected level of aggregate compaction, the shrinkage may vary between 10% and 30% of the cell volume.

To further enrich the structure, each cell is randomly shifted within the available surrounding space (see Figure 4c). Finally, to break the mutual parallelism of cell surfaces, each cell is rotated by a random 3D angle (see Figure 4d). During this process, we ensure that no two cells (grains) collide. In this way, a mesostructure resembling that of concrete is created; compare Figure 4e with Figure 3. A 3D illustration of the created structure is shown in Figures 5b and 5c.

For collision detection between grains, the Separating Axis Theorem (SAT) [26] is applied. The core idea of SAT is to identify if there exists an axis along which the projections of two polyhedra do not overlap. If such an axis is found, the polyhedra are not colliding; if no separating axis exists, a collision is detected.

The method begins by calculating the normal vectors (axes) for the faces of each polyhedron. These normals serve as potential separating axes. The vertices of the polyhedra are then projected onto these axes. If, for any axis, the projections do not overlap, the algorithm returns False, indicating no collision. If the projections overlap on all axes, the algorithm returns True, indicating a collision. This approach is efficient and widely used for detecting collisions between convex polyhedra. A schematic algorithm of the described mesostructure generation process is provided in Algorithm 1.

---

**Algorithm 1** Random Sequential Node Placement and Mesostructure Generation

---

**Input:** Domain  $\Omega$ , distance range  $[d_{\min}, d_{\max}]$ , target saturation  $S_{\text{target}}$

Initialize  $d \leftarrow d_{\max}$

Initialize node set  $N \leftarrow \emptyset$

**while** Saturation  $S < S_{\text{target}}$  **do**

failures  $\leftarrow 0$

**while** failures  $< 10^5$  **do**

Randomly generate node  $n \in \Omega$

**if**  $\forall m \in N, \|n - m\| \geq d$  **then**

Add  $n$  to  $N$

Update saturation  $S$

Reset failures  $\leftarrow 0$

**else**

Increment failures

**end if**

**end while**

Decrease  $d$  to the next value on the Fuller curve

**end while**

**Step 2: Shrink Cells**

**for** each cell  $C_i$  in the structure **do**

Compute center of gravity  $G_i$

Shrink  $C_i$  towards  $G_i$  by a factor  $s \in [10\%, 30\%]$

**end for**

**Step 3: Random Cell Shifting and Rotation**

**for** each cell  $C_i$  **do**

**while**  $C_i$  collides **do**

Randomly shift  $C_i$  within allowed bounds

Rotate  $C_i$  by a random 3D angle as a rigid body

Collision Detection Using SAT

**for** each already placed cell  $C_j$  **do**

Face normals as potential separating axes

Project vertices of  $C_i$  and  $C_j$  onto these axes

**if** any axis separates the projections **then**

No collision detected

Add  $C_i$  to the list of placed cells

**else**

Collision detected

Reattempt random shift and rotation for  $C_i$

**end if**

**end for**

**end while**

**end for**

**Output:** Generated mesostructure geometry

---

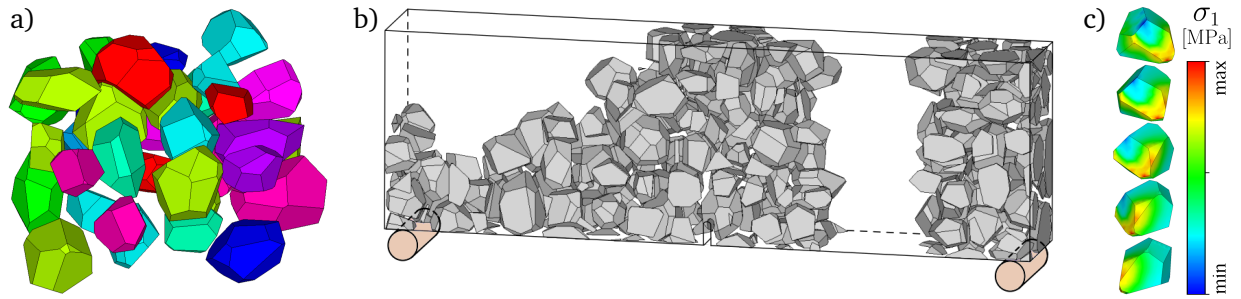


Figure 5: a) A 3D representation of aggregates, b) example of the mesostructure within a notched three-point bending specimen, c) exemplary  $\sigma_1$  stress field on the surface of an aggregate.

### 3.2. Meshing and preprocessing

The described mesostructure can be generated to fill the exact volume of the intended numerical model, or alternatively, the model can be extracted (cut) from a larger bulk material structure. This choice depends on whether the mesostructure near the model boundaries should reflect influences such as formwork or a specimen cut from the bulk material.

The resulting geometry and topology of the aggregate structure are imported into the ANSYS framework using the PyMAPDL library [27], where volume objects are created in accordance with the topology. For complex 3D topologies, mesh generation can constitute a significant portion of the total computational cost. The default ANSYS APDL mesher was found to be insufficient in terms of efficiency and performance. Therefore, we chose to employ the highly efficient Gmsh mesh generator [28], which offers significant improvements in both speed and flexibility. For volumetric meshing of the model, we use 20-node hexahedral SOLID186 elements (suitable for elastic analysis) that are degenerated into their tetrahedral forms. This approach is necessary to effectively mesh geometries with complex features, providing a balance between accuracy and computational feasibility. However, it is critical to carefully select the element size to avoid excessively large stress gradients within the model.

To optimize computational efficiency, regions of the model with expected low stress gradients are coarsened, see Figure 6. These areas exhibit minimal variations in stress distribution, allowing for mesh reduction without significant loss of accuracy. Such an approach was verified e.g. in [29].

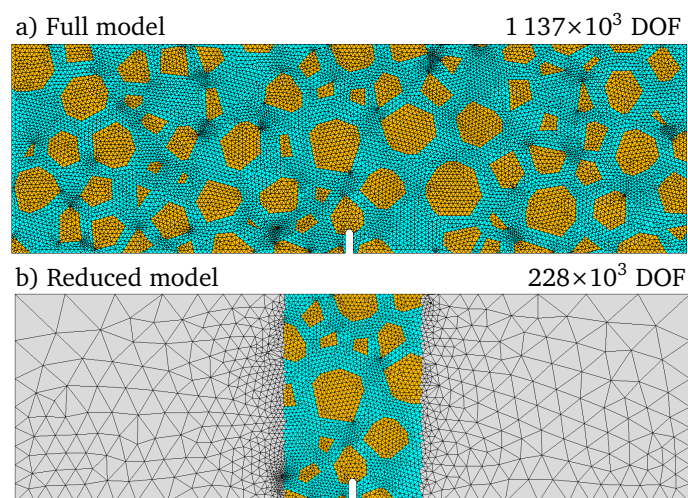


Figure 6: Reducing model complexity by coarsening regions with expected low stress gradients

In this work, without any noticeable loss of precision, computational demands were reduced by modeling and

finely meshing the mesostructure only within the inner 25% of the model width. In this fine-mesh region, the maximum element size was set to 2 mm (see the mesh study in Section Appendix A).

Within the left and right outer 37% of the model width, a coarser mesh was applied, representing a homogenized material with properties averaged between the cement matrix and aggregates. In this coarse region, the maximum element size was generally unrestricted, except for the support regions where it was limited to 6 mm to ensure adequate resolution.

The use of the efficient Gmsh library provides a substantial preprocessing speedup compared to the proprietary ANSYS mesher.

Subsequently, the assembled numerical models were executed on the computational resources of the Czech IT4Innovations National Supercomputing Center. This setup benefits from significant solution speedup due to the utilization of multiple multiprocessor computational nodes with extensive memory and storage capabilities.

Table 1: FEM Model Comparison

	Full model	Reduced model
Volume Elements	$2\,040 \times 10^3$	$406 \times 10^3$
Degrees of Freedom	$1\,137 \times 10^3$	$228 \times 10^3$
Gmsh Meshing	15 min	90 sec
ANSYS Solution	10 min	1.5 min
RAM Required	148 GB	41 GB
Energy Used	0.597 kWh	0.107 kWh
Energy Cost	0.15 EUR	0.03 EUR

Table 1 presents a comparison between the full and reduced finite element models in terms of computational efficiency, resource requirements, and energy consumption. The table lists the number of volume elements and degrees of freedom (DOFs) for each model, as well as the meshing time in Gmsh, the ANSYS solution time using 8 computation nodes (totaling 288 cores, i.e.,  $8 \times 2 \times 36$  cores of Intel Cascade Lake 6240), the RAM required for the in-core solution of the FEM problem, and the total energy consumed during computation.

The full model, shown in Figure 6a, consists of approximately 2.04 million volume elements and 1.137 million DOFs. It requires 15 minutes for meshing, 148 GB of RAM, and 16 minutes for the solution, consuming 0.597 kWh of energy. In contrast, the reduced model, shown in Figure 6b, contains 406 thousand volume elements and 228 thousand DOFs, significantly reducing computational cost with a meshing time of 90 seconds, a RAM requirement of 41 GB, and an ANSYS solution time of only 3 minutes, consuming 0.107 kWh.

In this work, 3D numerical models of typical concrete test specimens were created using the above-described mesoscale topology generation method. The following sections detail the modeling steps, focusing on specimen dimensions and boundary conditions.

## 4. Numerical models

In the text below, we present the geometries of the studied numerical models, including boundary conditions and analytical solutions of stress field distribution within several common concrete test specimen setups: an unnotched (blunt) three-point bending (Section 4.1), a notched three-point bending (Section 4.2), and a compressed cylinder (Section 4.3).

### 4.1. Blunt three-point bending setup

The first model is a standard unnotched (blunt) three-point bending specimen, illustrated in Figure 7 (unnotched variant). The test specimen has a span  $S = 240$  mm, depth  $D = 80$  mm, thickness  $T = 80$  mm.

The boundary conditions for the supports are modeled by creating rigid regions on the beam's bottom face (CERIG elements). Each rigid region is associated with a master node (MASS21), located at the region's center of gravity, shown in red in Figure 7. The distance between the two master support nodes corresponds exactly to the beam span  $S$ . At the supports, zero displacements are imposed in the  $y$ - and  $z$ -directions (denoted  $u_y = u_z = 0$ ), along with zero rotation about the  $X$ -axis and zero overall rotation of the model about the  $Y$ -axis. The loading master node is assigned a vertical force  $F_y = 1$  N to represent a unit load; its horizontal displacements  $u_x$  and  $u_z$  are constrained to zero.

For the blunt 3PBT geometry, the uniaxial normal stress component  $\sigma_x$  is examined, as it can be directly compared to the corresponding normal stress from Euler-Bernoulli beam theory. This comparison takes into account the statistical nature of the mesostructure, as discussed in Section 5.1.

The analytical solution for the normal stress distribution in a linear homogeneous material is:

$$\sigma_{x,LM} = \frac{FL}{4I} y, \quad (3)$$

where  $F$  is the applied force (unitary here),  $L$  is the beam span,  $I$  is the moment of inertia of the beam cross-section, and  $y$  is the vertical distance from the neutral axis.

However, relying solely on normal stress for damage assessment can be misleading, as fracture or damage initiation often occurs under multiaxial stress states, especially when the concrete mesostructure is explicitly modeled.

### 4.2. Notched three-point bending setup

A standard three-point bending test setup is used, encompassing both notched and unnotched variants. The test specimen has a span  $S = 240$  mm, depth  $D = 80$  mm, thickness  $T = 80$  mm, and, for the notched variant, a

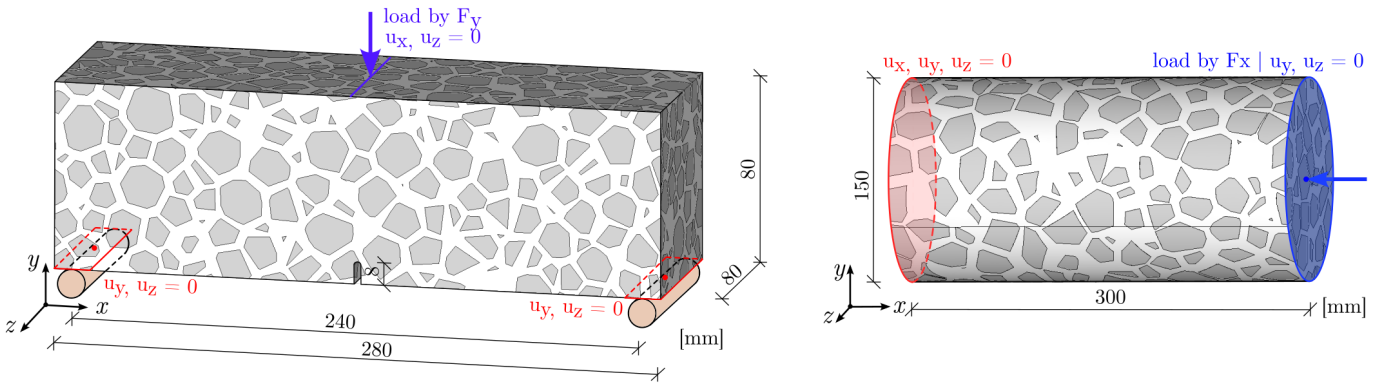


Figure 7: Boundary conditions and dimensions of 3D notched three point bending numerical model.

notch height  $a = 0.1D$ . The notch width is 3 mm and its tip is rounded, as illustrated in Figure 7. It is important to note that the stress values  $\sigma_{x_{LEFM}}$  are computed assuming a sharp notch tip, so strict numerical comparison with the rounded-tip model cannot be enforced.

The boundary conditions for the top load are modeled similarly to the blunt case. A narrow rigid region is created across the top surface of the model, with a master node assigned at its center. The loading master node is assigned a vertical force  $F_y = 1$  N representing a unit load, while its horizontal displacements  $u_x$  and  $u_z$  are constrained to zero.

The normal stress distribution within the 3D FEM model is compared to the response of a linear homogeneous material obtained from a 2D FEM counterpart model under plane strain conditions. This 2D model was employed to extract bending LEFM stress  $\sigma_{xx}$  along the specimen height  $W$ . To accurately capture the crack-tip singularity, the notch tip was meshed using the KSCON command, which collapses quadrilateral elements into triangular ones and moves mid-side nodes to one-quarter of the element length. The 2D mesh consisted of 8-node quadrilateral elements of type PLANE183. The 2D model dimensions, loading, and material parameters corresponded to those of the 3D mesoscale FEM model. The 2D numerical solution was validated against the analytical stress intensity factor  $K_I$  from [30], achieving an error below 1% [31]. After confirming the good agreement of  $K_I$ , the bending stress  $\sigma_{xx}$  was extracted for comparison. The results demonstrate that the most frequent stress values closely align with the analytical solution, with only minor low-frequency noise around these values.

### 4.3. Compression-loaded cylinder

The second test setup is a clamped compression-loaded cylinder with height  $H = 300$  mm and diameter  $D = 150$  mm. Rigid regions of nodes are created on both cylinder faces and assigned to their respective master nodes located at the geometric centers, as shown in Figure 7. The master node on the loaded (top) face (blue) is constrained in all rotations and displacements except for the vertical displacement load  $u_y$ . The master node on the supported (bottom) face (red) is fully restrained in all translations and rotations.

The normal stress distribution within the proposed FEM model is compared to the analytical solution for a linear homogeneous material:

$$\sigma_{x,LM} = \frac{N}{A}, \quad (4)$$

where  $N$  is the applied axial force (here unitary), and  $A$  is the cylinder cross-sectional area.

For a homogeneous material, the numerical model reproduces the expected mechanical response in terms of normal stress distribution as predicted by linear elastic fracture mechanics. Experimental studies reporting stress fluctuations under compression can be found in [32, 33, 34, 35].

## 5. Numerical results and discussion

The sections below detail the methodology used for numerical data analysis of the studied geometries. Special attention is given to the extraction of stress data from the simulation results for each geometry. We then present the local stress distribution within aggregates derived from the internal stress state. This is followed by an in-depth analysis of the influence of stiffness ratio on the stress field, including a statistical evaluation of this complex problem.

### 5.1. Numerical data analysis

To analyze the stress field in the models, we extract stress values from multiple parallel cross-sections along the specimen. The cross-sections are positioned sufficiently close relative to the specimen's scale to cover volumes experiencing similar mechanical load states. This allows us to treat the extracted stress values as representative of a single cross-section of finite thickness.

Without significant loss of information, we further condense the data by dividing the cross-section height into many thin layers, over which histograms of stress values are constructed. By assembling these histograms at their respective vertical positions, we obtain a comprehensive summary of the stress distribution across the investigated volume of the model.

This approach is illustrated in Figure 8 for a three-point bending test specimen. Figure 9 shows an example of the normal stress field across such a cross-section, highlighting differences between aggregate and matrix phases with unequal Young's moduli.

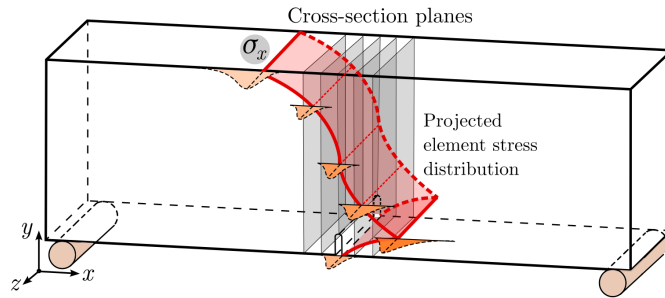


Figure 8: Cross-sectional planes used for statistical data analysis.

By this evaluation method, no information is lost or averaged out; the visualization preserves details on stress extremes as well as the full distribution of stresses.

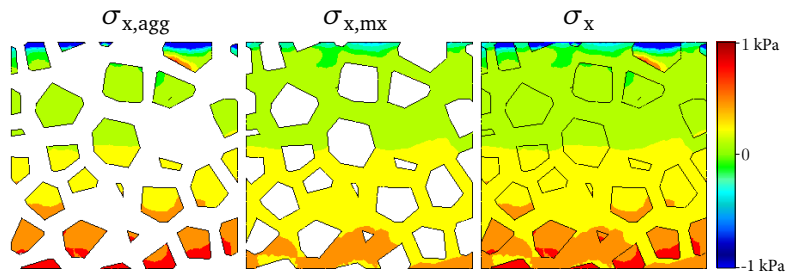


Figure 9: Normal stress across a 2D cross-section within the aggregate material ( $\sigma_{x,agg}$ ), matrix material ( $\sigma_{x,mx}$ ) and full cross-section ( $\sigma_x$ ).

The results presented below were acquired within 10 equidistant cross-sections spread across the notch width, extracted from 50 numerical models with unique aggregate structures.

## 5.2. Influence of Stiffness Contrast on Local Stress Distribution

To assess the effect of mesoscale stiffness heterogeneity on the internal stress state of concrete, we conducted an elastic finite element analysis focusing on a single polyhedral aggregate embedded within a continuous cementitious matrix. The first principal stress,  $\sigma_1$ , was evaluated under uniaxial loading conditions for varying stiffness ratios defined as  $R_{M/A} = E_{mx}/E_{agg}$ , ranging from 0.1 to 10. As illustrated in Figures 10 and 11, the stress field within the inclusion is highly sensitive to  $R_{M/A}$ .

For soft aggregates ( $R_{M/A} < 1$ ), the aggregate remains nearly stress-free, with the matrix accommodating the majority of the external load. Conversely, for  $R_{M/A} > 1$ , the aggregate attracts and concentrates stress, with pronounced localization of  $\sigma_1$  near sharp geometric features such as corners and edges, particularly at  $R_{M/A} = 5$  and  $R_{M/A} = 10$ .

This behavior aligns qualitatively with classical inclusion theory—specifically Eshelby’s solution for ellipsoidal inclusions in infinite media [36]. According to Eshelby, a homogeneous ellipsoidal inclusion embedded in a linearly elastic infinite matrix under uniform remote stress experiences a uniform internal stress and strain field, which can be expressed analytically. However, our case involves a faceted (polyhedral) inclusion with non-ellipsoidal geometry, where Eshelby’s assumptions no longer hold. In such cases, the internal stress field becomes non-uniform and exhibits singularities at geometric discontinuities. Analytical and numerical extensions, such as those presented in [37], confirm that polyhedral inclusions produce more complex stress fields, with stress intensification driven both by stiffness mismatch and inclusion geometry.

These findings highlight the pivotal role of stiffness contrast and morphological features in governing local stress distributions, which are central to the initiation of microcracks and the subsequent fracture evolution in quasi-brittle heterogeneous materials like concrete.

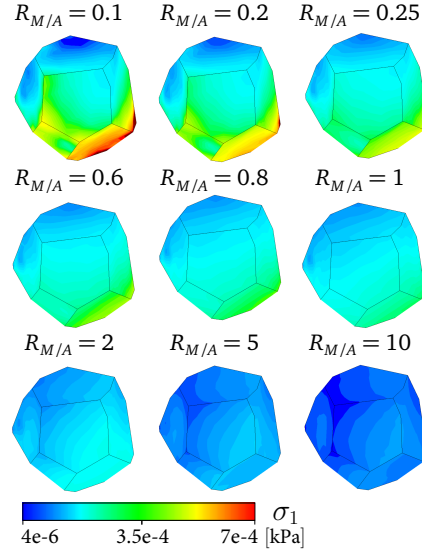


Figure 10: Development of the principal stress  $\sigma_1$  distribution on a grain surface as influenced by stiffness heterogeneity.

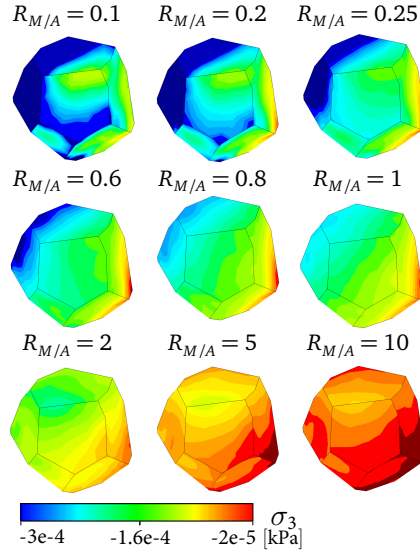


Figure 11: Development of the principal stress  $\sigma_3$  distribution on a grain surface as influenced by stiffness heterogeneity.

### 5.3. Stress field dependence on aggregate to matrix stiffness ratio

In what follows, we investigate the influence of increasing stiffness contrast between the aggregate and matrix material phases. The aim is to provide insight into how the stress distribution within the material evolves as the heterogeneity of material properties between the matrix and aggregate phases increases.

This investigation is particularly relevant for the utilization of alternative aggregate materials, such as recycled crushed bricks (see Section 2). The presence of inclusions significantly softer (lower Young’s modulus) than granite, or even softer than the cement matrix, can lead to substantial increases in stress concentrations within the composite. Such elevated stress concentrations are expected to cause earlier crack initiation during the service life compared to traditional granite aggregates. We believe that these numerical results contribute to a better understanding of concrete’s inherent heterogeneity and the resulting local stress concentrations.

We analyze the evolution of normal stress distribution differences between a homogeneous material and increasingly heterogeneous composites.

As noted in the introduction, the elastic modulus of aggregates can vary widely—from about 3.5 GPa (e.g., crushed bricks) up to 75 GPa or more (e.g., crushed granite). The cement matrix modulus typically ranges between 10 GPa and 30 GPa [38]. This results in stiffness ratios  $R_{M/A}$  spanning roughly from 0.1 to 10. More elastic properties of various materials can be found [39]. For this study, the Poisson’s ratio is fixed at  $\nu = 0.2$  for both materials. The aggregate structure is generated to resemble a realistic distribution of aggregate sizes between 2 and 16 mm.

The MFEM stress values are displayed as relative histograms across a fine array of layers along the specimen height. In each layer, dark red indicates the most frequent stress values, with frequency decreasing towards dark blue. For homogeneous models ( $R_{M/A} = 1$ ), the most frequent stress values closely match the analytical reference solution, with scattered noise of negligible frequency around these values. Only near the top surface of the TPB models do compressive stress concentrations appear due to the loading boundary condition.

When stiffnesses are comparable ( $R_{M/A} \approx 1$ ), strains in matrix and aggregates are compatible, resulting in a smooth stress distribution. However, as the heterogeneity becomes more pronounced in either direction, the normal stress distributions within matrix and aggregates diverge.

For a softer matrix relative to aggregates ( $R_{M/A} < 1$ ), stress peaks within the matrix tend to smear out because the matrix deforms more easily while transferring load between aggregates. Nonetheless, the matrix remains responsible for overall equilibrium, so its stress cannot approach zero.

Conversely, for softer aggregates relative to the matrix ( $R_{M/A} > 1$ ), the stiffer matrix attracts more stress due to its higher deformation resistance. As aggregate stiffness decreases, they lose the ability to effectively transfer stress across the composite, forcing the matrix to carry a larger portion of the load. In the limiting case, the composite behaves like a cement matrix with void inclusions.

This phenomenon is further illustrated in Figure 12, which shows maximum normalized normal stress quantiles,  $\bar{\sigma}_{x,\max}(q)$ :

$$\bar{\sigma}_{x,\max}(q) = \frac{\sigma_{x,\max,\text{hetero}}(q)}{\sigma_{x,\max,\text{homo}}(q)}, \quad (5)$$

where  $\sigma_{x,\max,\text{hetero}}(q)$  is the  $q$ th quantile of maximum normal stress in the heterogeneous material and  $\sigma_{x,\max,\text{homo}}(q)$  is the corresponding quantile for the homogeneous material ( $R_{M/A} = 1$ ).

The results clearly indicate that the most favorable stress distribution occurs when the stiffness of inclusions closely matches that of the matrix. In this balanced state, stress is more evenly shared between phases, minimizing localized concentrations that may trigger damage. Deviations from this balance—either with significantly softer or stiffer inclusions—lead to pronounced stress redistribution and localization, especially at interfaces and near sharp polyhedral features.

This effect is particularly critical when replacing conventional stiff aggregates, such as granite, with alternative materials for sustainability or cost reasons. The mechanical consequences of high stiffness contrast must be carefully assessed, as they may compromise the composite's structural integrity or durability. Our findings emphasize the importance of considering mesoscale mechanical compatibility—not just material availability—in the selection of aggregates for concrete design.

Figures 13 and 14 show the stress distribution in the blunt three-point bending (TPB) model within the matrix and aggregates, respectively. Similarly, Figures 15 and 16 present the stress distribution for the notched TPB model, again distinguishing between matrix and aggregates. Finally, Figures 15 and 18 depict the stress distribution in the compression-loaded cylinder model within matrix and aggregates, respectively.

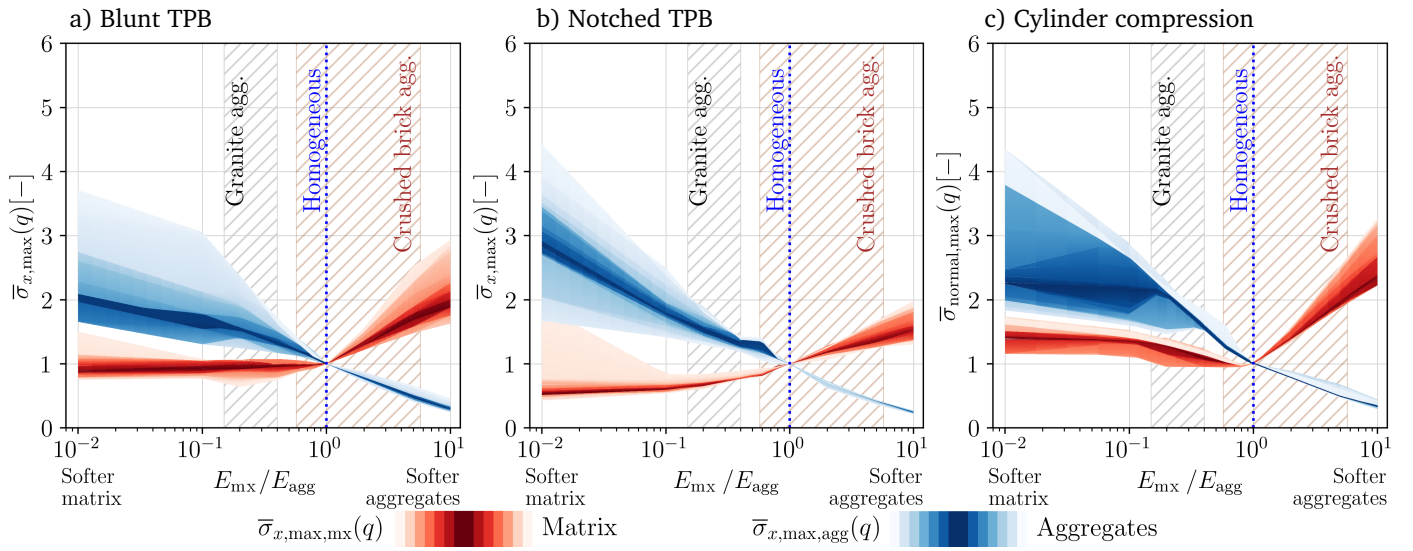


Figure 12: Normed normal stress quantiles  $\bar{\sigma}_{\text{Normal,max}}(q)$ .

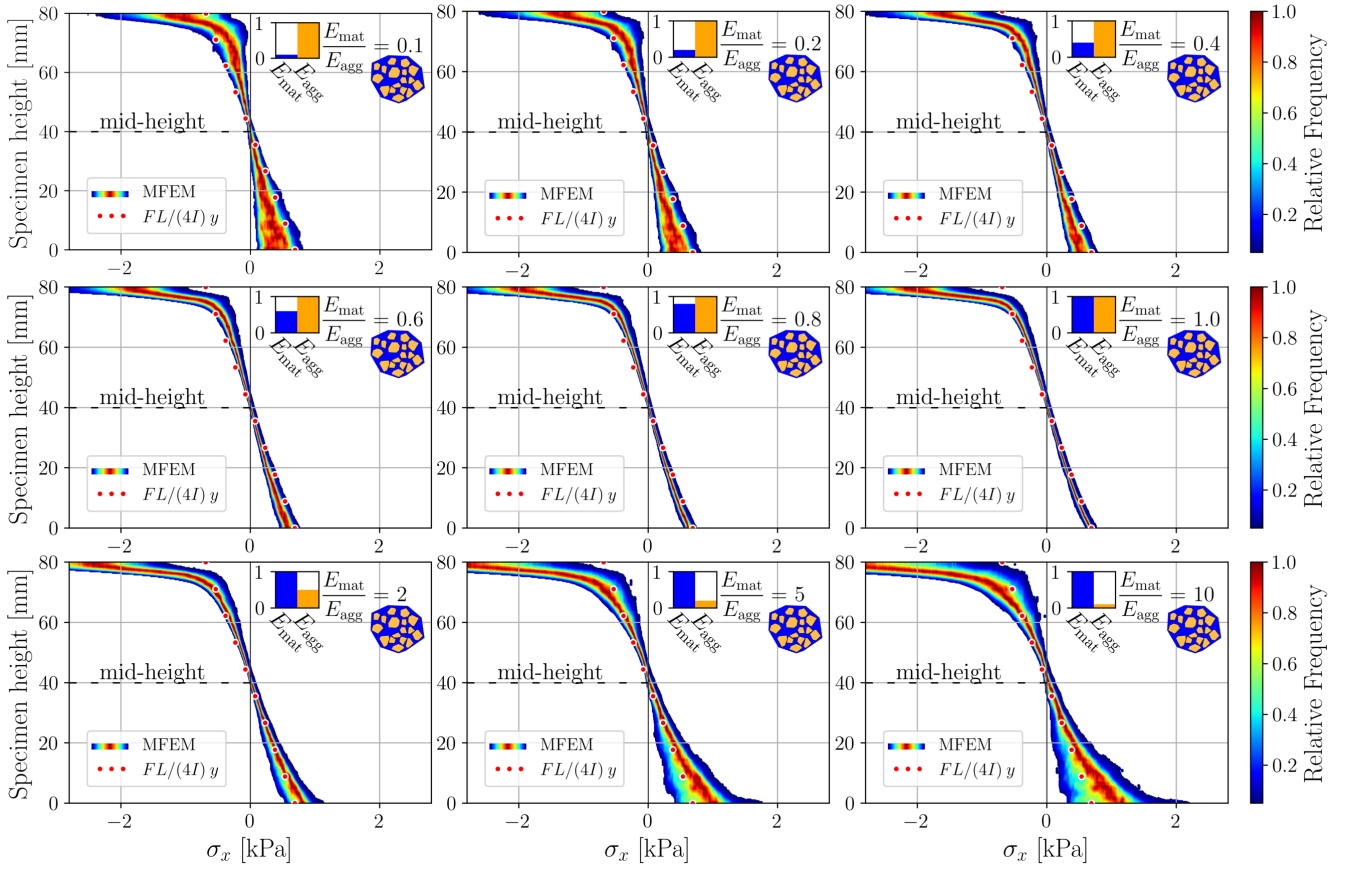


Figure 13: Blunt TPB: matrix normal stress within the notch region in dependence on the heterogeneity parameter,  $R_{M/A}$ .

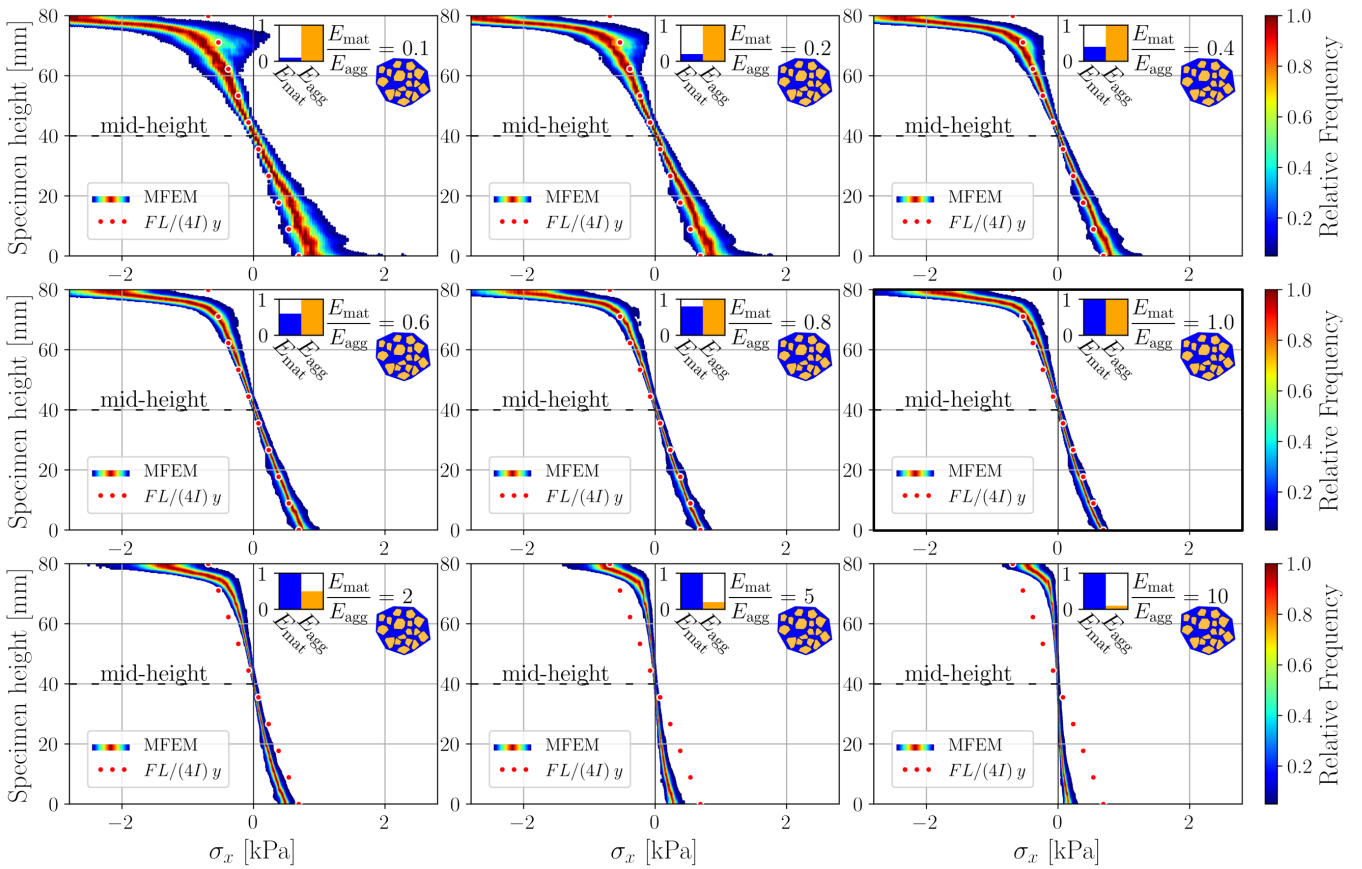


Figure 14: Blunt TPB: aggregates normal stress within the notch region in dependence on the heterogeneity parameter,  $R_{M/A}$ .

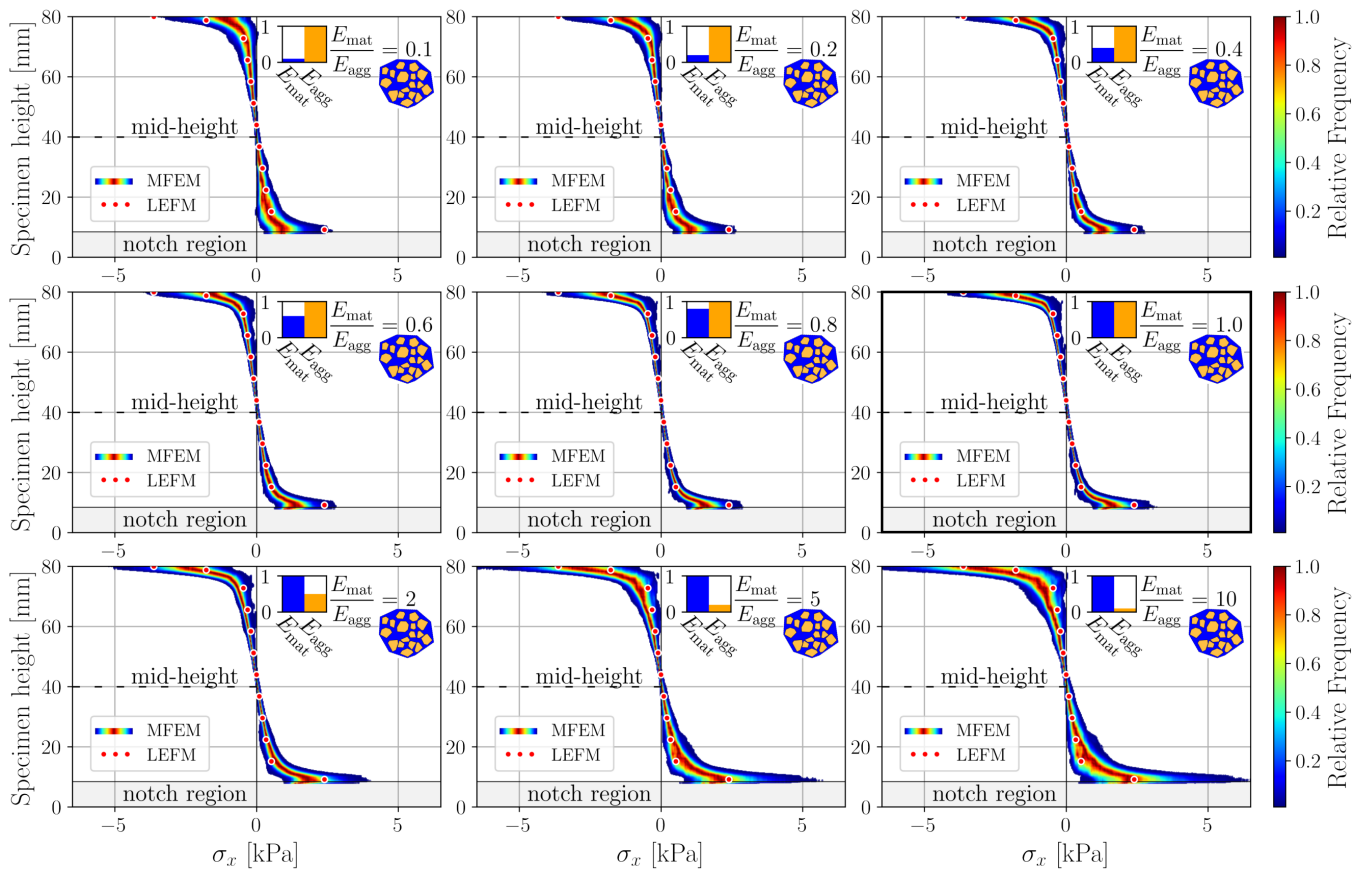


Figure 15: Notched TPB: matrix normal stress within the notch region in dependence on the heterogeneity parameter,  $R_{M/A}$ .

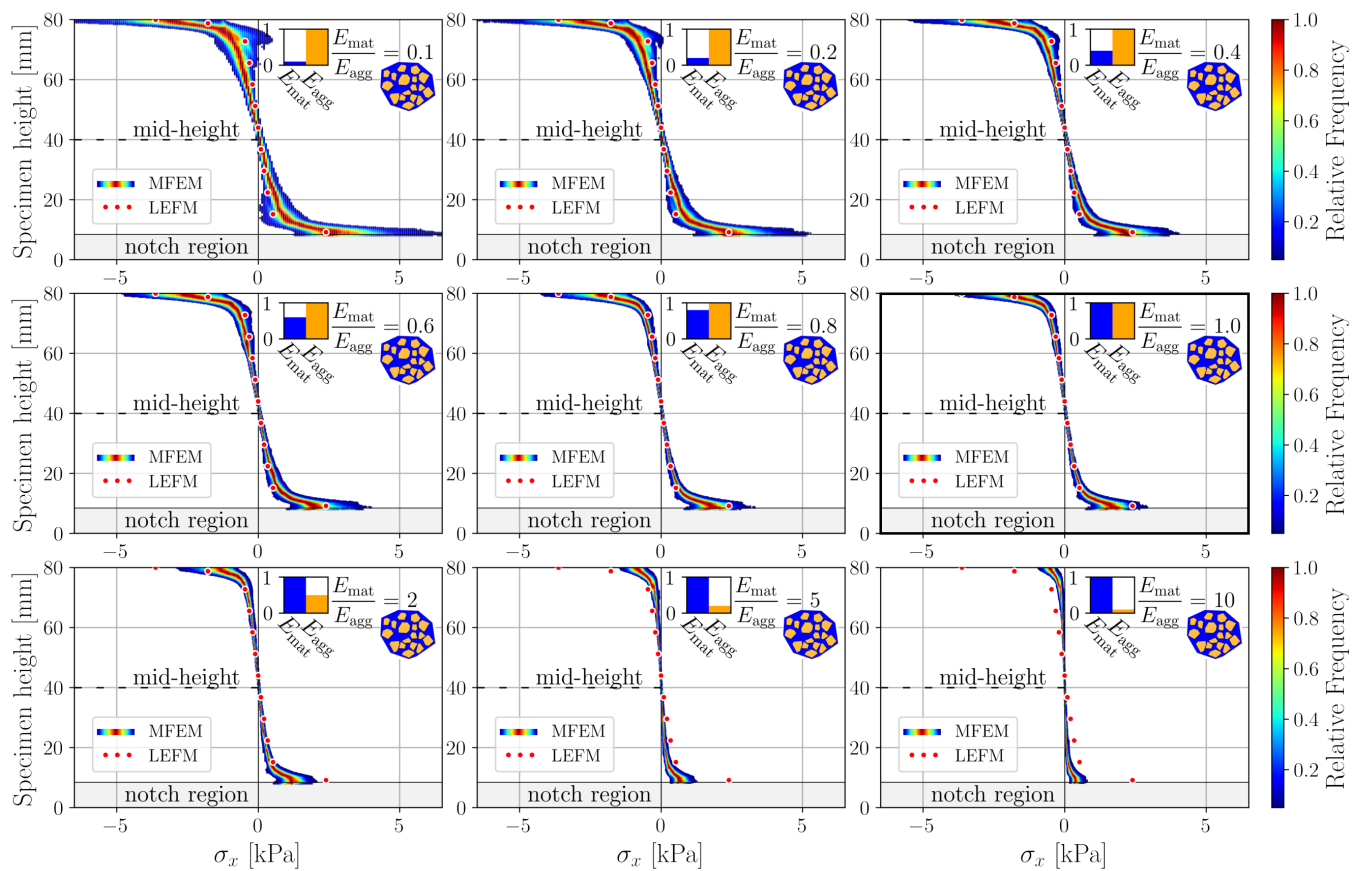


Figure 16: Notched TPB: aggregates normal stress within the notch region in dependence on the heterogeneity parameter,  $R_{M/A}$ .

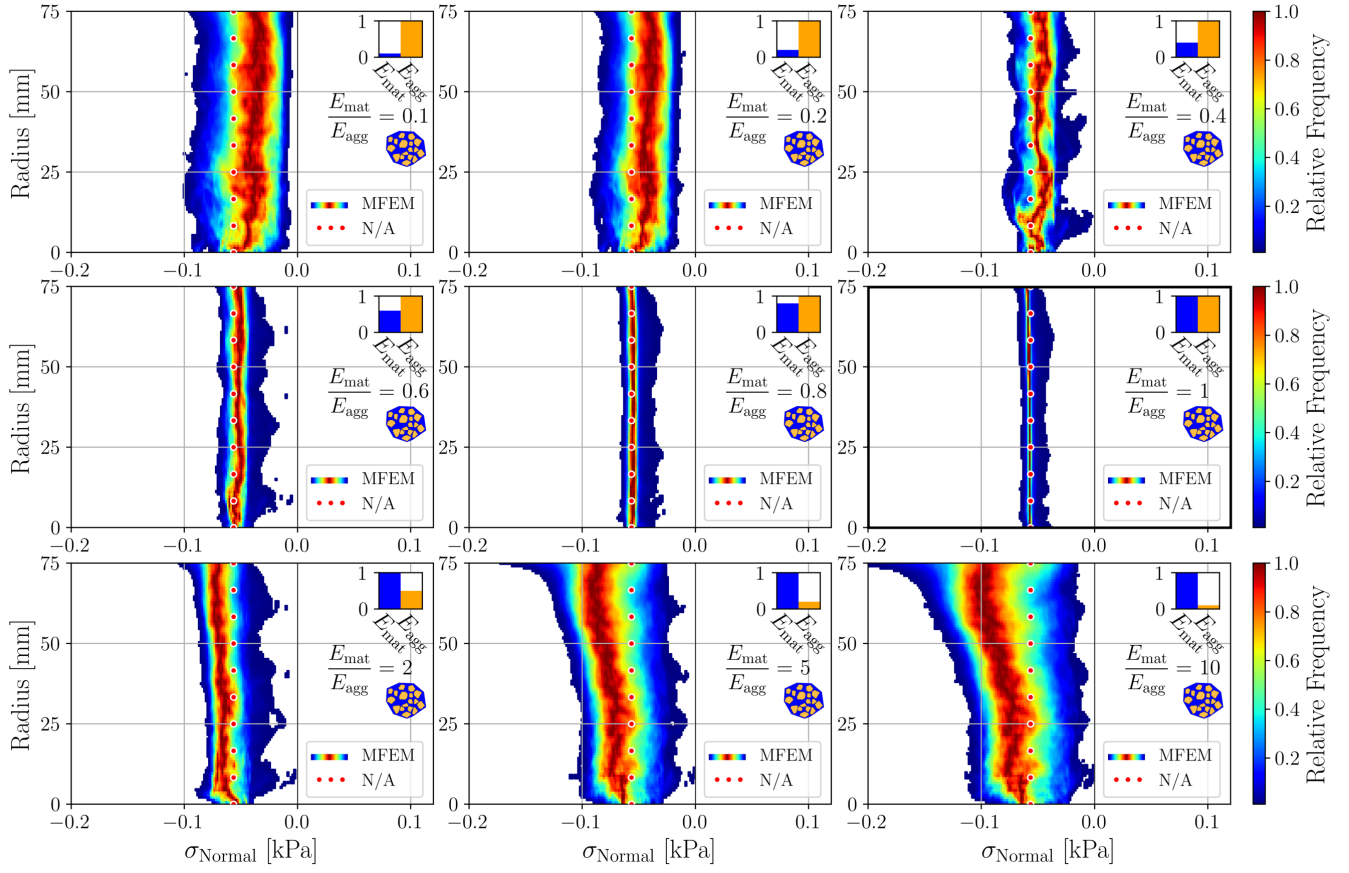


Figure 17: Cylinder compression: matrix normal stress  $\sigma$  at midspan region in dependence on the heterogeneity parameter,  $R_{M/A}$ .

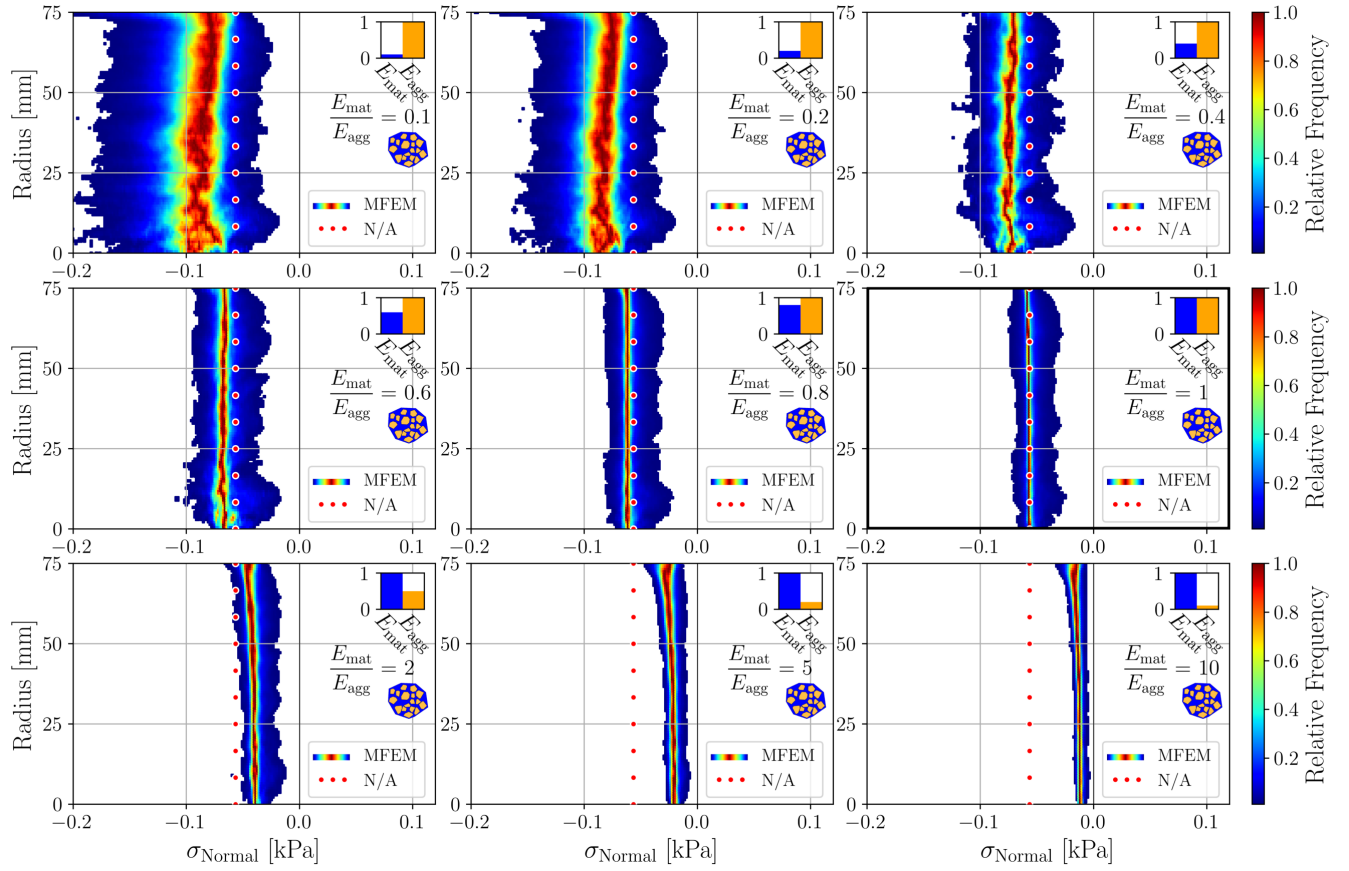


Figure 18: Cylinder compression: aggregates normal stress at midspan region in dependence on the heterogeneity parameter,  $R_{M/A}$ .

## 6. Conclusions

In the presented work, a Mesoscale Finite Element Model (MFEM) of concrete was developed, enabling detailed representation of its internal heterogeneity. Leveraging today's high-performance computing capabilities, the approach explicitly resolves the aggregate structure, offering a more transparent and versatile framework compared to existing models such as LDPM. This fine-resolution modeling is particularly suitable for investigating the influence of mesoscale mechanical contrasts on stress distribution and failure mechanisms—an area of growing relevance with the increasing interest in sustainable, non-traditional aggregates such as crushed brick recycle.

The study focused on evaluating the effects of varying the stiffness ratio between the aggregate and matrix phases on the stress field and potential failure processes within the composite. The results reveal that the relative stiffness of these constituents plays a decisive role in governing internal stress redistribution and damage evolution.

When the stiffness ratio approaches unity, the phases exhibit compatible deformation behavior, resulting in a smooth and uniform stress distribution. As the stiffness mismatch increases, two distinct regimes emerge:

- **Stiff aggregates in a soft matrix:** The compliant matrix undergoes larger deformations, promoting stress redistribution over a wider region. This tends to reduce local stress concentrations but compromises the overall stiffness of the composite. While aggregates continue to serve as load-bearing elements, excessive matrix deformation may promote early microcracking, especially under fatigue or cyclic loading.
- **Soft aggregates in a stiff matrix:** The stiff matrix bears the majority of the load, leading to localized stress peaks at matrix-aggregate interfaces. In this regime, the aggregates no longer contribute effectively to load transfer, and may act as stress concentrators rather than reinforcements. This increases the likelihood of crack initiation and propagation, often leading to brittle failure mechanisms. In the extreme case, the behavior resembles that of a matrix containing voids, with significantly impaired structural resilience.

These observations underline the importance of maintaining a balanced stiffness contrast between the phases. Ideally, aggregate materials with mechanical properties comparable to those of the matrix are preferred, as they ensure efficient load sharing and minimal stress localization. When replacing traditional stiff aggregates like granite with more compliant or recycled materials, such as crushed bricks, these mechanical drawbacks must be carefully assessed to avoid unintended reductions in structural integrity or durability.

Overall, the MFEM approach provides valuable insights into mesoscale interactions in concrete and sets the stage for further exploration of nonlinear phenomena, damage localization, and the optimization of alternative composite designs.

## 7. Acknowledgement

This paper was created as part of the project No. CZ.02.01.01/00/22\_008/0004631 Materials and technologies for sustainable development within the OP JAK Program financed by the European Union and from the state budget of the Czech Republic. Numerical calculations were done within the IT4Innovations National Supercomputing Center, Czech Republic supported by the Ministry of Education, Youth and Sports of the Czech Republic through the e-INFRA CZ (ID:90254).

### Data Availability

The data used in this study is available at: <https://doi.org/10.5281/zenodo.15640474>.

## References

- [1] E. G. Nawy, *Fundamentals of high-performance concrete*, John Wiley & Sons, 2000.
- [2] E. C. for Standardization, *En 1992-1-1: Eurocode 2: Design of concrete structures - part 1-1: General rules and rules for buildings* (2004).  
URL <https://www.cen.eu>
- [3] K. L. Scrivener, K. M. Nemati, The percolation of pore space in the cement paste/aggregate interfacial zone of concrete, *Cement and concrete research* 26 (1) (1996) 35–40.
- [4] K. L. Scrivener, A. K. Crumbie, P. Laugesen, The interfacial transition zone (itz) between cement paste and aggregate in concrete, *Interface science* 12 (2004) 411–421.
- [5] Z. Hashin, P. Monteiro, An inverse method to determine the elastic properties of the interphase between the aggregate and the cement paste, *Cement and Concrete Research* 32 (8) (2002) 1291–1300.
- [6] J. Lee, G. L. Fenves, Plastic-damage model for cyclic loading of concrete structures, *Journal of engineering mechanics* 124 (8) (1998) 892–900.
- [7] J. Červenka, V. K. Papanikolaou, Three dimensional combined fracture–plastic material model for concrete, *International journal of plasticity* 24 (12) (2008) 2192–2220.
- [8] F. C. Caner, Z. P. Bažant, Microplane model m7 for plain concrete. i: Formulation, *Journal of Engineering Mechanics* 139 (12) (2013) 1714–1723.
- [9] I. Zreid, M. Kaliske, A gradient enhanced plasticity–damage microplane model for concrete, *Computational Mechanics* 62 (5) (2018) 1239–1257.
- [10] Z.-J. Yang, B.-B. Li, J.-Y. Wu, X-ray computed tomography images based phase-field modeling of mesoscopic failure in concrete, *Engineering Fracture Mechanics* 208 (2019) 151–170.
- [11] P. Wriggers, S. Moftah, Mesoscale models for concrete: Homogenisation and damage behaviour, *Finite elements in analysis and design* 42 (7) (2006) 623–636.
- [12] M. Nitka, J. Tejchman, Meso-mechanical modelling of damage in concrete using discrete element method with porous itzs of defined width around aggregates, *Engineering Fracture Mechanics* 231 (2020) 107029.
- [13] E. A. Rodrigues, O. L. Manzoli, L. A. Bitencourt Jr, 3d concurrent multiscale model for crack propagation in concrete, *Computer Methods in Applied Mechanics and Engineering* 361 (2020) 112813.
- [14] G. Cusatis, D. Pelessone, A. Mencarelli, Lattice discrete particle model (ldpm) for failure behavior of concrete. i: Theory, *Cement and Concrete Composites* 33 (9) (2011) 881–890.
- [15] A. A. Munjiza, *The combined finite-discrete element method*, John Wiley & Sons, 2004.
- [16] P. C. Paris, G. C. Sih, Stress analysis of cracks, *ASTM stp 381* (1965) 30–81.
- [17] T. L. Anderson, T. L. Anderson, *Fracture mechanics: fundamentals and applications*, CRC press, 2005.
- [18] A. Hillerborg, M. Modéer, P.-E. Petersson, Analysis of crack formation and crack growth in concrete by means of fracture mechanics and finite elements, *Cement and concrete research* 6 (6) (1976) 773–781.
- [19] M. Jirasek, Nonlocal models for damage and fracture: comparison of approaches, *International Journal of Solids and Structures* 35 (31-32) (1998) 4133–4145.
- [20] J. Xiao, W. Li, D. J. Corr, S. P. Shah, Effects of interfacial transition zones on the stress–strain behavior of modeled recycled aggregate concrete, *Cement and Concrete Research* 52 (2013) 82–99.
- [21] J. Xiao, W. Li, Z. Sun, D. A. Lange, S. P. Shah, Properties of interfacial transition zones in recycled aggregate concrete tested by nanoindentation, *Cement and Concrete Composites* 37 (2013) 276–292.
- [22] R. V. Silva, J. De Brito, R. K. Dhir, Establishing a relationship between modulus of elasticity and compressive strength of recycled aggregate concrete, *Journal of cleaner production* 112 (2016) 2171–2186.
- [23] M. Adamson, A. Razmjoo, A. Poursaee, Durability of concrete incorporating crushed brick as coarse aggregate, *Construction and building materials* 94 (2015) 426–432.
- [24] S. Narayanan, M. Sirajuddin, Properties of brick masonry for fe modeling, *American Journal of Engineering Research* 1 (2013) (2013) 6–11.
- [25] F. Aurenhammer, Power diagrams: properties, algorithms and applications, *SIAM journal on computing* 16 (1) (1987) 78–96.
- [26] W. contributors, Hyperplane separation theorem — wikipedia, the free encyclopedia, accessed: 2025-01-28 (2025).  
URL [https://en.wikipedia.org/wiki/Hyperplane\\_separation\\_theorem](https://en.wikipedia.org/wiki/Hyperplane_separation_theorem)
- [27] A. Kaszynski, *pyansys: Pythonic interface to MAPDL* (Nov. 2021). doi:10.5281/zenodo.4009466.  
URL <https://doi.org/10.5281/zenodo.4009466>

- [28] C. Geuzaine, J.-F. Remacle, Gmsh: A 3-d finite element mesh generator with built-in pre-and post-processing facilities, *International journal for numerical methods in engineering* 79 (11) (2009) 1309–1331.
- [29] J. Mašek, J. Květoň, J. Eliáš, Adaptive discretization refinement for discrete models of coupled mechanics and mass transport in concrete, *Construction and Building Materials* 395 (2023) 132243.
- [30] H. Tada, P. C. Paris, G. R. Irwin, The stress analysis of cracks, *Handbook*, Del Research Corporation 34 (1973) (1973).
- [31] S. Blasón, T. Werner, J. Kruse, M. Madia, P. Miarka, S. Seitzl, M. Benedetti, Determination of fatigue crack growth in the near-threshold regime using small-scale specimens, *Theoretical and applied fracture mechanics* 118 (2022) 103224.
- [32] R. Hurley, D. Pagan, An in-situ study of stress evolution and fracture growth during compression of concrete, *International Journal of Solids and Structures* 168 (2019) 26–40.
- [33] C. Perry, J. Gillott, The influence of mortar-aggregate bond strength on the behaviour of concrete in uniaxial compression, *Cement and Concrete Research* 7 (5) (1977) 553–564.
- [34] M. B. Cil, K. A. Alshibli, 3d evolution of sand fracture under 1d compression, *Géotechnique* 64 (5) (2014) 351–364.
- [35] M. B. Cil, K. A. Alshibli, P. Kenesei, 3d experimental measurement of lattice strain and fracture behavior of sand particles using synchrotron x-ray diffraction and tomography, *Journal of Geotechnical and Geoenvironmental Engineering* 143 (9) (2017) 04017048.
- [36] J. D. Eshelby, The determination of the elastic field of an ellipsoidal inclusion, and related problems, *Proceedings of the Royal Society of London. Series A. Mathematical and Physical Sciences* 241 (1226) (1957) 376–396. doi : 10.1098/rspa.1957.0133.
- [37] G. J. Rodin, Eshelby's inclusion problem for polygons and polyhedra, *Journal of the Mechanics and Physics of Solids* 44 (12) (1996) 1977–1995. doi : 10.1016/S0022-5096(96)00066-X.
- [38] D. Wei, R. C. Hurley, L. H. Poh, D. Dias-da Costa, Y. Gan, The role of particle morphology on concrete fracture behaviour: A meso-scale modelling approach, *Cement and Concrete Research* 134 (2020) 106096.
- [39] J. D. Bass, et al., Elasticity of minerals, glasses, and melts, *Mineral physics and crystallography: A handbook of physical constants* 2 (1995) 45–63.

## Appendix A. Notes on mesh density

The accuracy and reliability of FEM-based numerical models are often influenced by mesh sensitivity, necessitating an appropriate mesh size to achieve both high-quality results and feasible computational efficiency. In this study, the level of physical discretization within each model is determined by the size and placement of the aggregates. The generated mesh consists of 3D tetrahedral elements, chosen for their compatibility with the complex geometries of the aggregates while ensuring numerical stability. Since the analysis is purely elastic, the primary objective is to accurately capture stress distributions without accounting for nonlinearities such as cracking or plasticity. The mesh is generated using Gmsh, which provides control over element quality and ensures a well-conditioned discretization. Additionally, mesh optimization (Mesh.Optimize) is applied to improve element shapes and enhance numerical stability. Mesh density is manually controlled through the maximum element size,  $l_{\max}$ , to impose sufficient refinement in the notch vicinity.

A mesh convergence study was performed to determine an optimal element size, ensuring that computed stress fields and displacement responses remained consistent across successive refinements. The final mesh configuration balances accuracy and computational cost, capturing essential features of the elastic stress distribution without excessive computational overhead. The optimal mesh size was verified before proceeding with further numerical analysis and was subsequently adopted. This mesh study was conducted using a three-point bending test model (see Section 4.2). Several progressively finer meshes were examined, as summarized in Tab.A.2.

Due to the inherent complexity of the model, the prescribed maximum element size cannot always be strictly maintained. Regions with intricate geometries or sharp features require finer elements to ensure proper mesh generation. In such cases, the meshing algorithm automatically reduces element size to maintain quality and prevent element distortion. As a result, while the specified maximum element size serves as a guideline, local refinements occur where necessary to accommodate the model's geometric constraints.

$l_{\max}$	n.o. Elements [-]	n.o. DOF [-]
1 mm	$2\,150 \times 10^3$	$1\,140 \times 10^3$
2 mm	$435 \times 10^3$	$305 \times 10^3$
3 mm	$232 \times 10^3$	$696 \times 10^3$
5 mm	$160 \times 10^3$	$480 \times 10^3$
10 mm	$158 \times 10^3$	$474 \times 10^3$

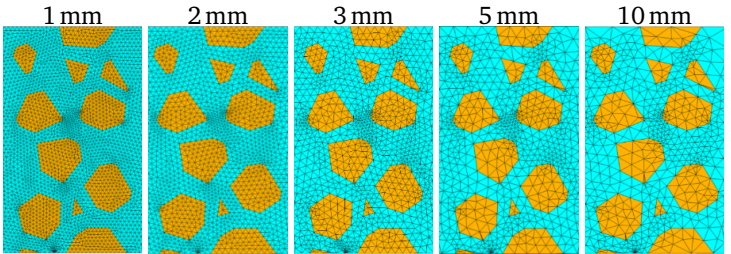


Table A.2: Mesh study: midspan mesh of the TPB Model.

The study was conducted on a three-point bending beam model, and the obtained stress distribution was compared to the analytical solution. Convergence was examined by progressively refining the mesh from coarser to finer resolutions. First row of Figure A.19 shows the respective normal stress histograms of each studied mesh. The second row shows the absolute error,  $\epsilon(\sigma_x)$ , of each model envelopes respective to the analytical solution.

The results indicate that a 1 mm element size was excessively fine, leading to a substantial increase in computational cost without a proportional improvement in accuracy. Conversely, the 2 mm mesh provided sufficient precision in capturing stress distributions while maintaining a reasonable computational expense. The differences were within acceptable limits, confirming that the chosen discretization effectively captured the expected stress behavior. Following the convergence study, a mesh with a maximum element size of 2 mm was selected for subsequent analyses. The 2 mm mesh provided sufficient precision in capturing stress distributions while avoiding excessive computational costs associated with finer discretizations. A further reduction in element size would have significantly increased the computational burden without yielding substantial improvements in accuracy.

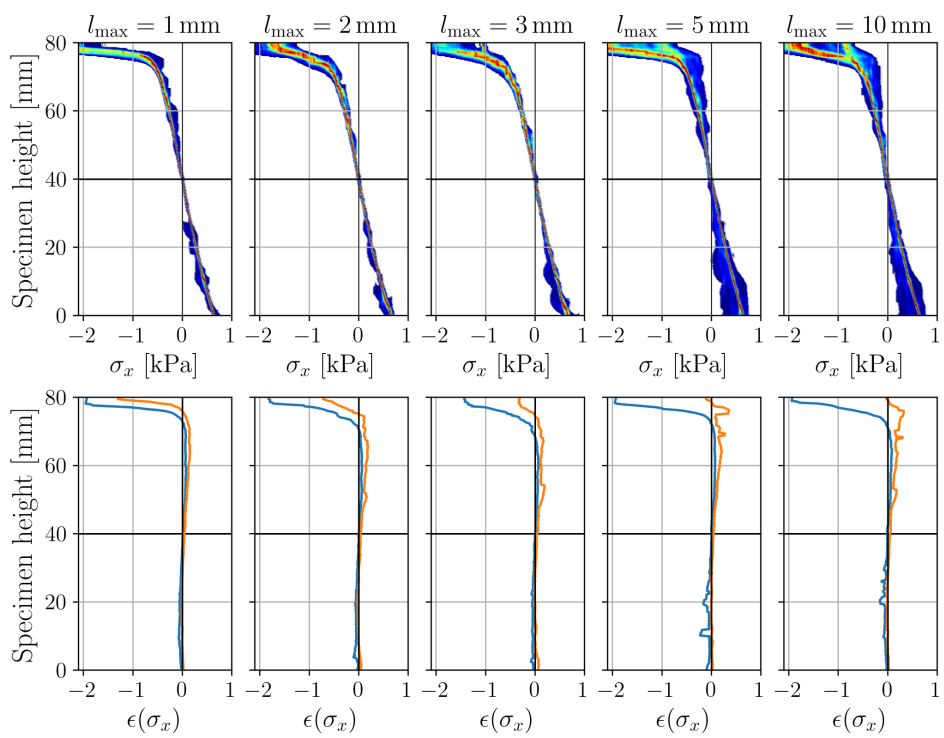


Figure A.19: Mesh error study